This document is downloaded from DR-NTU (https://dr.ntu.edu.sg)
Nanyang Technological University, Singapore.

Spinel Co3O4 nanomaterials for efficient and stable large area carbon-based printed perovskite solar cells

Bashir, Amna; Shukla, Sudhanshu; Lew, Jia Haur; Shukla, Shashwat; Bruno, Annalisa; Gupta, Disha; Baikie, Tom; Patidar, Rahul; Akhter, Zareen; Priyadarshi, Anish; Mathews, Nripan; Mhaisalkar, Subodh Gautam

2017

Bashir, A., Shukla, S., Lew, J. H., Shukla, S., Bruno, A., Gupta, D., . . . Mhaisalkar, S. G. (2018). Spinel Co3O4 nanomaterials for efficient and stable large area carbon-based printed perovskite solar cells. Nanoscale, 10(5), 2341-2350. doi:10.1039/c7nr08289d

https://hdl.handle.net/10356/141121

https://doi.org/10.1039/c7nr08289d

© 2018 The Royal Society of Chemistry. All rights reserved. This paper was published in Nanoscale and is made available with permission of The Royal Society of Chemistry.

Downloaded on 27 Aug 2022 03:23:43 SGT

Spinel Co_3O_4 nanomaterials for efficient and stable large area carbon-based printed perovskite solar cells

Amna Bashir,[a,c] Sudhanshu Shukla,[a] Jia Haur Lew,[a] Shashwat Shukla,[a] Annalisa Bruno,[a] Disha Gupta,[b] Tom Baikie,[a] Rahul Patidar,[a,d] Zareen Akhter,[c] Anish Priyadarshi, *[a] Nripan Mathews [a,b] and Subodh G. Mhaisalkar *[a,b]

Carbon based perovskite solar cells (PSCs) are fabricated through easily scalable screen printing techniques, using abundant and cheap carbon to replace the hole transport material (HTM) and the gold electrode further reduces costs, and carbon acts as a moisture repellent that helps in maintaining the stability of the underlying perovskite active layer. An inorganic interlayer of spinel cobaltite oxides (Co_3O_4) can greatly enhance the carbon based PSC performance by suppressing charge recombination and extracting holes efficiently. The main focus of this research work is to investigate the effectiveness of Co_3O_4 spinel oxide as the hole transporting interlayer for carbon based perovskite solar cells (PSCs). In these types of PSCs, the power conversion efficiency (PCE) is restricted by the charge carrier transport and recombination processes at the carbon–perovskite interface. The spinel Co_3O_4 nanoparticles are synthesized using the chemical precipitation method, and characterized by X-ray diffraction (XRD), X-ray absorption spectroscopy (XAS), field emission scanning electron microscopy (FESEM), transmission electron microscopy (TEM) and UV-Vis spectroscopy. A screen printed thin layer of p-type inorganic spinel Co_3O_4 in carbon PSCs provides a better-energy level matching, superior efficiency, and stability. Compared to standard carbon PSCs (PCE of 11.25%) an improved PCE of 13.27% with long-term stability, up to 2500 hours under ambient conditions, is achieved. Finally, the fabrication of a monolithic perovskite module is demonstrated, having an active area of 70 cm^2 and showing a power conversion efficiency of >11% with virtually no hysteresis. This indicates that Co_3O_4 is a promising interlayer for efficient and stable large area carbon PSCs

Introduction

Hybrid organic–inorganic lead halide perovskites ($CH_3NH_3PbX_3$; X = I, Br and Cl) (methylammonium lead halide) have emerged as a promising material for a wide range of optoelectronic applications such as solar cells, light emitting devices and laser cooling due to their excellent semiconducting properties.[1–4] These materials can be easily synthesized through facile solution processing routes due to their propensity towards rapid crystallization which yields nearly defect-free and highly crystalline films with exceptional carrier diffusion lengths and theoretical carrier mobilities up to 100 $cm^2\ V^{-1}\ s^{-1}$ and a high optical absorption coefficient of $\sim 10^5$ cm^{-1}.[5–9] This has led to unprecedented progress in the perovskite solar cell efficiencies in recent years, since the initial reports of 3% to the current lab scale record efficiency of 22.1%.[10,11] Pathways pursued to enhance the efficiency include crystal quality improvement via solvent engineering,[12] improved device architecture,[13] increasing grain size,[14,15] compositional variation[16] and optimizing electron (ETL) and hole

transporting layers (HTL) and with additives.[17–19]

Recently, printable carbon-based electrodes have shown to play a promising role for scale up and stable perovskite solar cells using printing technology.[20–25] These devices are remarkably stable for >3 months under ambient conditions (25 °C and 60% RH) without encapsulating it but the efficiency of the standard carbon-based PSC is still below 15%.[21,22] Favourable band energetics of the perovskite valence band position with carbon, together with its ambipolar nature, facilitates hole transfer through a carbon layer.[23] In addition, the carbon layer also acts as a moisture barrier and prevents the hydration of the perovskite absorber, therefore substantially reducing the degradation kinetics. Despite such advantages, the performance of carbon based perovskite solar cells is limited by the interface charge transfer. Moreover, charge carrier extraction by the carbon electrode alone is not as efficient as in the case of conventional HTL based PSCs.[26] Strategies to improve the carbon–perovskite interface with a thin inorganic HTL film could be an efficient way of improving the charge transport to achieve higher efficiencies. Nickel oxide (NiO_x), as an inorganic hole conductor layer, was printed before carbon to improve the hole extraction in the hole-conductor free perovskite solar cells.[27–29] This improves the carrier extraction from the perovskite and passivates the interfacial defect/trap states. Despite the beneficial advantages of using a NiO layer, the conductivity still remains low which results in a poor fill factor (FF) and low current density (J_{sc}). Alternatives to NiO are p-type oxide spinels, that are promising hole transporting materials due to their excellent hole conductivity and mobility.[30–33]

In this paper, we report the use of p-type cobalt oxide, Co_3O_4 for enhancing the hole transport in carbon based perovskite solar cells for the first time. Cobalt oxide (Co_3O_4) belongs to the Fd3m space group and has a conventional cubic spinel crystal structure with high-spin Co^{2+} ions in the tetrahedral sites and low-spin Co^{3+} ions in the octahedral sites of the cubic close-packed lattice of oxygen anions. The valence band position of Co_3O_4 (−5.3 eV) matches better with a low lying valence band of the perovskite (∼−5.4 eV), favouring efficient hole extraction from the perovskite layer.[34]

Co_3O_4 nanoparticles were synthesized by chemical precipitation and characterized by X-ray diffraction (XRD), transmission electron microscopy (TEM) and XAS (X-ray absorption spectroscopy). A thin Co_3O_4 layer was deposited using a scalable screen printing process to enhance the hole extraction in carbon based PSCs. The charge extraction properties of the printed spinel Co_3O_4 layer were investigated using photoluminescence (PL) quenching and Time Resolved PL (TRPL) experiments. The performance of the perovskite solar cell was evaluated using a solar simulator, and electrochemical impedance spectroscopy (EIS).

Synthesis and structural characterization of Co_3O_4 nanoparticles and paste

Various nanostructures of Co_3O_4 including nanowires,[35] nanoflakes,[36] nanotubes[37] and hollow spheres[38] have been synthesized successfully, but there are still several challenges observed in these synthetic routes, such as the tendency of Co_3O_4 to grow into large and irregular particles. To control particle growth, and to prevent these undesirable processes, organic surfactants are often used.[39,40] However, the use of organic surfactants increases the cost and is not environmentally friendly.[41] The other challenge is the control over the phase purity of the final product during the low temperature synthesis of Co_3O_4. Hence, from a practical and a green chemistry point of view, there is a need to develop a simple and reliable synthetic route to single phase Co_3O_4 nanomaterials without the use of organic surfactants.

In this work we have synthesized Co_3O_4 nanoparticles, using a chemical precipitation method similar to that reported by Deng et al.[42] This method does not involve the use of surfactants or templates, which makes it more environmentally friendly and reduces impurities in the final product.

$Co(NO_3)_2 \cdot 6H_2O$ (12.885 g) was dissolved in 100 mL of deionized water under magnetic stirring for two hours to make a homogeneous precursor solution. This aqueous solution of Co $(NO_3)_2 \cdot 6H_2O$ was treated with an alkali (10 M NaOH) under continuous stirring, to precipitate cobalt hydroxide. Following this, the precipitate was centrifuged, and washed five times with deionized water and ethanol to ensure there were no residual impurities. The obtained precipitate was further dried at 80 °C overnight followed by manual grinding (mortar and pestle for five minutes) and then transformed to the desired Co_3O_4 phase by thermal decomposition at 450 °C. The resultant Co_3O_4 nanoparticles were collected and characterized using the techniques described below.

Fig. 1(a) shows the XRD pattern of the Co_3O_4 nanoparticles. It can be observed that all the reflections from the sample can be indexed to a normal cubic spinel Co_3O_4 phase which are in good accordance with the standard cards of database ICDD PDF4+; reference no. – 01-080-1545. The diffraction peaks at 19.16°, 31.31°, 36.81°, 38.52°, 44.93°, 55.74°, 59.72° and 65.27° can be correspondingly denoted as (111), (220),

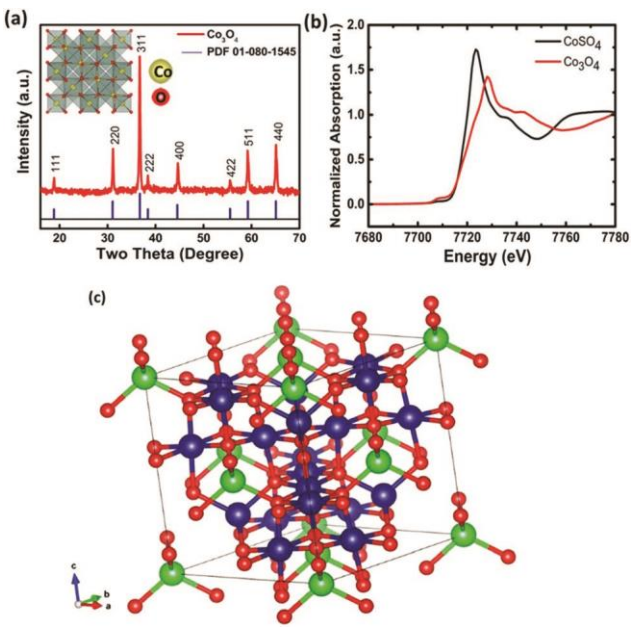

Fig. 1 (a) XRD pattern of Co_3O_4 nanoparticles, (b) XANES of Co_3O_4 (red) and $CoSO_4$ (black); (c) spinel structure of Co_3O_4. The green atoms correspond to the Co^{2+} tetrahedral sites while the blue ones are the Co^{3+} octahedral sites.

(311), (222), (400), (422), (511), and (440) reflection. The diffraction peaks confirm the presence of a pure nano-Co_3O_4 phase without $Co(OH)_2$ or other impurities. The experimental pattern along with the calculated pattern obtained from Rietveld refinement is shown in Fig. S1.† The difference curves show that the experimental pattern and calculated pattern are in good agreement. Rietveld refinement of the experimental diffractogram suggested a crystalline size of 34.9(9) nm and a lattice parameter of 8.0852(7), which closely matches with the cell constants documented in the ICDD PDF4+ database (reference no. – 01-080-1545). Fig. 1(a) also shows a nearly horizontal difference curve indicating a high-quality fit, which is further substantiated by a low value of Bragg's factor ($R_B = 0.1$).

X-ray absorption spectroscopy (XAS) measurements at the Co K edge (7709 eV) were carried out at the XAFCA[43] beamline of the Singapore Synchrotron Light Source (SSLS). Fig. 1(b) shows the Co K-edge XANES for Co_3O_4 and $CoSO_4$ (as a reference). $CoSO_4$ has cobalt present in the oxidation state Co^{2+}, whereas for Co_3O_4 we see a shift of almost 4.5 eV towards a higher energy which denotes that the oxidation state of cobalt in Co_3O_4 is higher than Co^{2+}. This is expected since the structure of Co_3O_4 is similar to the spinel structure of Fe_3O_4. Co_3O_4 has Co^{2+} ions occupying the tetrahedral sites surrounded by four oxygen atoms, while Co^{3+} ions are present in the octahedral sites with six oxygen atoms surrounding it.[43] The crystallographic file for Co_3O_4 used as a reference[44] in our XAS studies shows a similar structure as shown in Fig. 1(c). The pre-edge features in Co_3O_4 around 7707 eV correspond to the 1s–3d transitions which are prominent only for tetrahedrally coordinated metal atoms but forbidden for octahedral sites as they have a centre of inversion.[45,46] $CoSO_4$ has Co^{2+} octahedrally bonded to 6 surrounding oxygen atoms hence the pre-edge feature is missing in $CoSO_4$. Therefore, the peak in Co_3O_4 arises because of the Co^{2+} atoms present in the tetrahedral sites. Again, the sharp main peak intensity of $CoSO_4$ around 7723 eV is typical of the Co^{2+} complex due to which it is more obvious in $CoSO_4$ than Co_3O_4.

A more quantitative investigation was carried out with the first shell analysis of the EXAFS data to determine the correlation between the atomic distances of Co with its nearest neighbour (Fig. 2a and b). Table 1 shows the EXAFS results for the Co_3O_4 powder. Since there are two different cobalt sites, the analysis was conducted twice, once for each site. The tetrahedral bond length obtained was around 1.914 Å, and the octahedral bond length was 1.899 Å. The similarity of these values could suggest that the individual interactions from each valence state cannot be extracted from the data and the analysis yields an average Co–O bond length from the Co^{2+} and Co^{3+} two different sites. Indeed, the refined value is consistent with an average of the expected values from Co^{2+} and Co^{3+} bonded to oxygen in one tetrahedral and two octahedral sites respectively (cf. $Co^{2+}O_4 \approx$ 1.956 Å & $Co^{3+}O_6 \approx$ 1.903 Å).[42] Although the refined individual tetrahedral bond length is expected to be longer than the octahedral bond

since the oxidation state on the tetrahedral site is lower than the octahedral site.

Further insight into the morphology and microstructure of Co_3O_4 nanoparticles was gained by TEM and HRTEM. Fig. 2(c) and (d) show the bright-field and high-resolution TEM micrographs of Co_3O_4 synthesized nanoparticles respectively. Consistent with XRD, TEM results indicate that the microstructure comprises of spherical Co_3O_4 nanoparticles with the d spacing = 4.117 Å, along the (002) plane in this case.

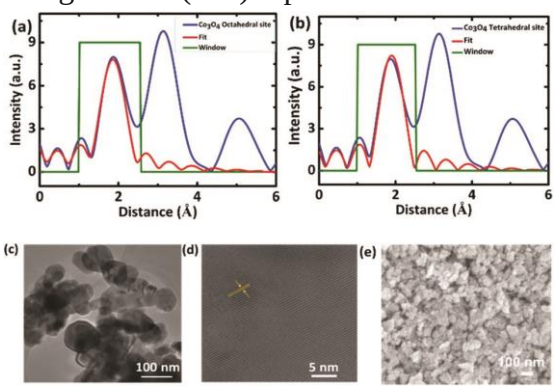

Fig. 2 EXAFS Fourier transform analysis for the (a) octahedral and (b) tetrahedral cobalt sites; (c) TEM image of the Co_3O_4 nanoparticles; (d) lattice fringes observed from the HRTEM image of Co_3O_4; (e) top-view SEM image of the screen printed Co_3O_4 film.

Following the synthesis and characterization of the Co_3O_4 nanoparticles, these particles were mixed with terpineol and ethyl cellulose to prepare a paste for screen printing on the glass substrate (as detailed in the Experimental section). The Co_3O_4 film was characterized using SEM and XRD techniques to understand any changes in the morphology and structural features during the process of thermal annealing to form the film. Fig. 2(e) shows the top-view SEM micrograph of the screen-printed film on the glass substrate. As preferred for perovskite solar cell fabrication, the film morphology appears to be mesoporous with agglomerated spherical nanoparticles of Co_3O_4. The XRD pattern of the screen-printed film (Fig. S2†) revealed that the crystal structure remains unchanged for the printed Co_3O_4 film. The diffraction patterns of nanoparticles and the screen-printed film are in perfect agreement including the peak position and intensity.

Fig. S3(a)† shows the optical absorption spectra of the screen printed Co_3O_4 film on glass. The data were recorded in the wavelength range of 300–900 nm. The first band (I) (λ = 413 nm) was attributed to the ligand to the metal charge transfer process in $O^{2-} \rightarrow Co^{2+}$, while the band (II) at a higher wavelength (λ = 719 nm) is due to the charge transfer process between $O^{2-} \rightarrow Co^{3+}$.[47] These two absorption bands additionally confirm the presence of Co^{2+} and Co^{3+} in the sample. The absorption band gap energy can be determined from the absorption spectra using the equation given below

$$(\alpha h\nu)^n = B'(h\nu - Eg)$$

Here hν is the photon energy in eV, B′ is the constant relative to the material, Eg is the band gap, α is the absorption coefficient and exponent n has different values depending on the electronic transitions in the material (2 for the direct allowed transitions, 1/2 for indirect allowed transitions and 2/3 for direct forbidden transitions). Fig. S3(b)† shows the variation of (αhν)2 versus (hν) for the screen printed Co3O4 film. Two band gaps for the

Table 1 Bond length data obtained from the analyses of XAS parameters based on the Co K-edge for Co_3O_4

Co_3O_4	Bond	CN	SO_2	σ^2 (Å^2)	$E°$ (eV)	Delr (Å)	R_{eff} (Å)	R (Å)
Co-tetrahedral site	Co–O1	4	0.915	0.002	−1.417	−0.042	1.956	1.914
Co-octahedral site	Co–O1	6	0.915	0.006	−5.206	−0.004	1.903	1.899

CN co-ordination number, SO_2 amplitude factor, σ^2 EXAFS Debye–Waller factor or disorder factor, R – bond distance.

Co_3O_4 sample suggest the direct allowed transitions (1.49 eV and 2.1 eV), which can be understood by keeping the band structure of Co3O4 in view. The valence band of Co3O4 has strong O 2p character, while $Co_{(II)}$ 3d orbitals are the main contributors to the conduction band. The $Co_{(III)}$ in Co3O4 gives rise to the sub-band located inside the energy gap. So E_{g1} (2.1 eV) represents the band gap corresponding to the $O^{2-} \rightarrow Co^{3+}$ transitions, while E_{g2} (1.49 eV) is the "true" band gap due to the inter-band transitions (valence to conduction band transitions).[30]

The electrical properties of the screen printed Co_3O_4 film were determined using a four-point probe station and the result from this is summarized in Table S1.† The conductivity of the screen-printed film is lower compared with the previous reports on Co_3O_4, which might be due to the mesoporous nature of the screen printed film.[30] Fig. 3a and b show the energy band offsets of different layers and the schematic of the solar cell for carbon based perovskite solar cells with a thin layer of spinel cobalt oxide, respectively. The valence band position of Co_3O_4 (~−5.3 eV) is higher than that of carbon (~−5.1 eV), and quite close to the valence band of the perovskite (~−5.4 eV).[34] Thus, cobalt oxide has a VBM compatible with the perovskite, which can facilitate efficient hole charge transfer. We conducted photoluminescence (PL) measurements to investigate whether Co_3O_4 along with carbon efficiently extracts photo-generated carriers from the perovskite absorber. Photoluminescence quenching from the $MAPbI_3/Co_3O_4/C$ layer on glass is shown in Fig. 3(c).

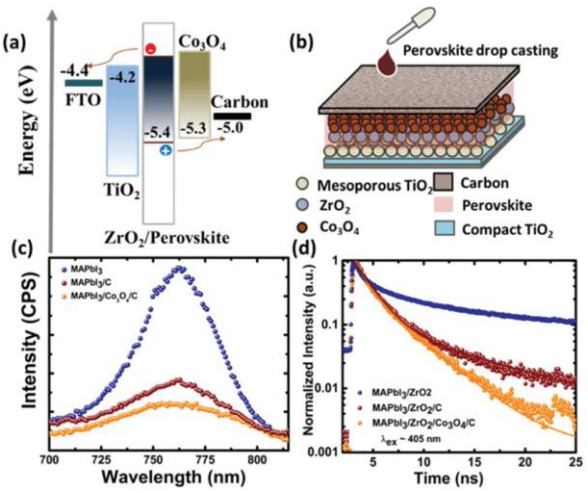

Fig. 3 (a) Energy band diagram, (b) schematic illustration of the device architecture, (c) photoluminescence (PL) spectra of pristine $MAPbI_3$, $MAPbI_3/C$ and $MAPbI_3/Co_3O_4/C$ on glass, (d) transient PL (TrPL) of $MAPbI_3/ZrO_2$ and $MAPbI_3/ZrO_2/C$ and $MAPbI_3/ZrO_2/Co3O_4/C$ on glass.

In the absence of any hole transporting layer, the $MAPbI_3$ film alone gave a characteristic PL spectrum with a broad peak centred around 760 nm corresponding to its bandgap. For the $MAPbI_3/Co_3O_4/C$ film, PL emission was strongly suppressed, indicating the more efficient extraction of holes from the perovskite compared with the $MAPbI_3/C$. In order to evaluate the interfacial carrier dynamics, we further resorted to time resolved PL measurements of the same film i.e. a

$MAPbI_3$ film on glass and a film with glass/$MAPbI_3$/Co_3O_4 (Fig. S4†). The decay curve is fitted with a bi-exponential decay function to obtain the relaxation lifetimes. An average decay time of 5.5 ns and 4.7 ns is obtained for the perovskite and $MAPbI_3$/Co_3O_4 film respectively. A shorter characteristic decay time for the $MAPbI_3$/Co_3O_4 film indicates efficient charge transfer from the perovskite to Co_3O_4.

In order to gain quantitative information on the yield of light induced charge separation in the device architecture (Fig. 3b) a PL decay study was carried out on $MAPbI_3$/ZrO_2, $MAPbI_3$/ZrO_2/C and $MAPbI_3$/ZrO_2/Co_3O_4/C films on the glass substrate with $MAPbI_3$ infiltrated from the top. The ZrO_2 acts as a reference because its conduction band is not suitable for hole injection. Fig. 3(d) shows the PL decay curve for the above-mentioned films on the glass. The decay curve is fitted with a bi-exponential decay function to obtain the relaxation lifetimes. The PL decay of $MAPbI_3$ contained in the ZrO_2 film exhibits a time constant of 8.4 ns, whereas for $MAPbI_3$/ZrO_2/C and $MAPbI_3$/ZrO_2/Co_3O_4/C it is 5.4 and 2.8 ns respectively. A shorter characteristic decay time for the film containing Co_3O_4 indicates that a more efficient charge transfer is possible for carbon based perovskite devices by adding an ultrathin layer of Co_3O_4 before carbon. Thus, both steady-state and time resolved PL quenching manifests an improved charge transfer for carbon due to the thin Co_3O_4 layer.

Perovskite solar cell fabrication and photovoltaic performance

We printed a thin layer of spinel cobaltite oxide in the carbonbased perovskite solar cell before the carbon electrode printing to understand its impact on the photovoltaic performance of the device. The solar cell architecture for the current study (Fig. 3b) is similar to that of our previous report on carbon based perovskite solar cells.[40] The perovskite solar cell comprises a thin compact layer of TiO_2 which serves as a blocking layer, followed by a mesoporous TiO_2 layer of (around 500 nm), ZrO_2 (1.3 μm), Co_3O_4 (less than 150 nm) and carbon (10–12 micron) layers. The perovskite solution was infiltrated through the carbon layer by manually dripping the solution by using a micropipette. The infiltrated perovskite solution seeps through the stack of carbon and mesoporous layers of Co_3O_4, ZrO_2 and TiO_2. Distinct layers are clearly visible from the cross-section SEM micrograph of the solar cell, as shown in Fig. 4a and b.

Device performance was optimized by varying the thickness of Co_3O_4 and ZrO_2 for the PSCs. The thickness of Co_3O_4 and ZrO_2 is varied by diluting the original Co_3O_4 paste (which gives an ~530 nm thick layer) and ZrO_2 paste (~1.4 μm) with the terpineol solvent. The cross-sectional SEM micrographs for different dilutions of Co_3O_4 are shown in Fig. S5.† The photovoltaic performances of the PSC for different thicknesses of Co_3O_4 and ZrO_2 are presented in Tables S2 and S3.† The best solar performance was achieved with a thin Co_3O_4 layer (with 1 : 5 dilution) and a thicker layer of ZrO_2 (1.3 μm). This optimized thickness of

cobalt oxide and ZrO_2 is considered for all perovskite solar cell fabrication in this paper.

The device performance of the perovskite–carbon solar cells with and without the (standard) Co_3O_4 layer is evaluated by analysing current density versus voltage (J–V) characteristics under 1 sun (100 mW cm^{-2}) light illumination, as shown in Fig. 4(c). With a Co_3O_4 thin layer, a V_{oc} of 0.88 V, a J_{sc} of 23.43 mA cm^{-2} and a FF of 0.64 leading to an overall efficiency of 13.27% (device area = 0.09 cm^2 after masking) were achieved. The corresponding solar cell parameters are tabulated in Table 2. Fig. S6(a)† shows the J–V curve for both the types of devices without any masking (an active area of 0.8 cm^2) and the corresponding cell parameters are tabulated in Fig. S6(b).†

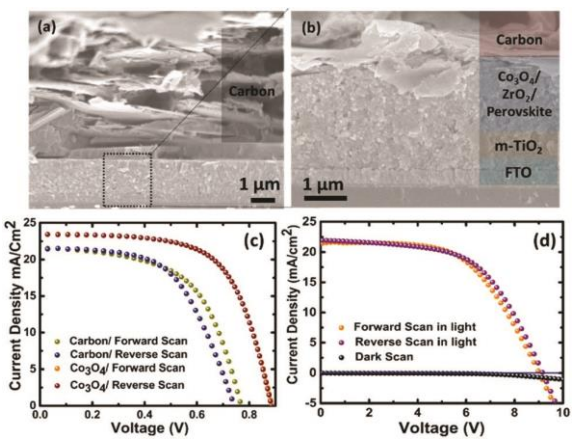

Fig. 4 (a) Low magnification and (b) high magnification cross-section SEM micrographs of the perovskite/carbon solar cell with a cobalt oxide layer, (c) J–V characteristics of the standard carbon cell without and with the Co_3O_4 (Co_3O_4/C) layer with an aperture area of 0.09 cm^2 under 1 sun (100 mW cm^{-2}) light illumination, (d) J–V characteristics of the standard carbon cell with the Co_3O_4 (Co_3O_4/C) layer with an active area of 70 cm^2 under 1 sun (100 mW cm^{-2}) light illumination.

Table 2 Solar cell parameters for the standard carbon cell without and with the Co_3O_4 layer with an active area of 0.09 cm^2 under 1 sun (100 mW cm^{-2}) light illumination

	Without Co_3O_4		With Co_3O_4	
Parameters	Reverse	Forward	Reverse	Forward
V_{oc} (V)	8.87	8.20	9.15	9.01
J_{sc} (mA cm^{-2})	21.28	19.50	22.10	20.85
FF	0.51	0.54	0.57	0.59
PCE (%)	9.75	8.75	11.39	11.06

Perovskite solar cells with Co_3O_4 exhibit more than a 2% increment in the efficiency compared to the standard perovskite solar cell with carbon alone. The better performance could stem from the fact that the deep lying VB of Co_3O_4 (−5.3 eV) forms a better ohmic contact with the perovskite layer, resulting in a large potential difference between the hole and electron transport layers. This suggests that the Co_3O_4 layer increases the hole collection at the carbon electrode.

Moreover, the Co_3O_4 cell showed negligible hysteresis in the forward and backward sweep of the J–V curve. There are reports on the critical role of the perovskite-contact interface in device hysteresis in perovskite solar cells. It is correlated to the combined effect of ion migration and recombination from the interfacial trap states. Thus, a better contact ultimately helps in mitigating the trap density, leading to less interfacial recombination and consequently reduces hysteresis.[48–50] To confirm the reproducibility of the PSC performance with Co_3O_4, fourteen devices with the Co_3O_4 layer were tested with an active area of 0.8 cm^2. The corresponding histogram is shown in Fig. S7,† whereas the average values for the device parameters are demonstrated in Table S4.†

The devices with the Co_3O_4 layer give significantly higher reproducibility with an average PCE value of 10.55 ± 0.69%.

We fabricated solar cells with an active area of 70 cm^2 to assure the scalability of the spinel cobaltite oxide method. These modules were fabricated using a semi-automated screen printing process which can be tuned according to the industrial needs. The current–density–voltage (J–V) characteristics of the perovskite solar module (PSM) of 70 cm^2 are shown in Fig. 4(d) and summarized in Table 3. All measurements were performed under standard reporting conditions (AM 1.5G) without any masking. The champion module delivers an efficiency of 11.39%, with an improved V_{oc} of 9.15 V as compared to carbon only (8.87 V), a J_{sc} of 22.10 mA cm^{-2} and a FF of 56.70%. Clearly a better performance is observed for devices containing the spinel Co_3O_4 interlayer because of better hole collection in these perovskite solar cells.

Table 3 Solar cell parameters for standard carbon cell with Co_3O_4 layer with an active area of 70 cm^2 under 1 sun (100 mW cm^{-2}) light illumination

	Without Co_3O_4		With Co_3O_4	
Parameters	Reverse	Forward	Reverse	Forward
V_{oc} (V)	8.87	8.20	9.15	9.01
J_{sc} (mA cm^{-2})	21.28	19.50	22.10	20.85
FF	0.51	0.54	0.57	0.59
PCE (%)	9.75	8.75	11.39	11.06

Analysis of the device performance

Impedance spectroscopy (IS) is a useful technique to characterize the charge transfer processes across the semiconducting interfaces and is widely adopted to study the carrier transport and recombination mechanisms in perovskite solar cells. Impedance spectra of the cells both with and without Co_3O_4 in the dark showed similar spectral features (Fig. S8(a)†) with a semicircle arc at a high frequency. Typical carrier transport and dynamics in a carbon-based perovskite cell comprises charge transfer processes at the cathode (TiO_2/perovskite interface), and at the anode (carbon/perovskite interface) and recombination within the active layer. However, a single distinct semicircle (corresponding to the single RC element) is obtained in the Nyquist plot and it is generally attributed to the charge transfer at the carbon/perovskite interface (hole injection or extraction). This is because the charge transfer resistance at the TiO_2/perovskite interface should be too small to be detected due to the fast electron injection, significantly large contact area and better interface contact.[51–53] A smaller semicircle is obtained for the cell with the Co_3O_4 layer indicating a lower charge transfer resistance from the perovskite to the Co_3O_4 interface which is responsible for the improved fill factor of the device.

By fitting the IS results using the equivalent circuit as shown in Fig. S8(a)† to extract the charge transfer resistance (R_{ct}).[54] Furthermore, the impedance measurements were performed at different operating voltages and plotted the corresponding values of R_{ct} extracted by fitting the individual Nyquist plots, as shown in Fig. 5a. R_{ct} values remain smaller for the Co_3O_4/C cell throughout the operational voltage window. This indicates the better charge carrier rate and improved interfacial recombination by the inclusion of the Co_3O_4

layer. Furthermore, EIS measurements were also conducted under 1 sun illumination under the frequency range from 1 MHz to 1 Hz at different applied biases (0.1 V to 1 V) to study the recombination resistance in devices both with and without Co_3O_4. Fig. S8(b)† presents the EIS Nyquist plots for devices both with and without Co_3O_4. The Nyquist plots showed two distinct semicircles. The first arc at a high frequency is related to the hole transport process between the perovskite and carbon counter electrode, corresponding to the charge transfer resistance (R_{ct}). The second arc in the middle frequency region is attributed to the recombination resistance (R_{rec}). Similarly, by fitting the individual Nyquist plots at different applied biases using the equivalent circuit shown in Fig. S8(b),† we obtain R_{rec} and R_{ct} (Fig. 5(b and c)). This indicates the better charge carrier rate and improved interface by the inclusion of the Co_3O_4 layer. This was attributed to an increasing FF.[55] On the contrary, the largest R_{rec} in the Co_3O_4/C device could explain the increase in the V_{oc} by C/ perovskite heterojunction engineering (Fig. 5c).[56] R_{ct} values remain smaller for the Co_3O_4/C cell at all values of applied potential (Fig. 5b).

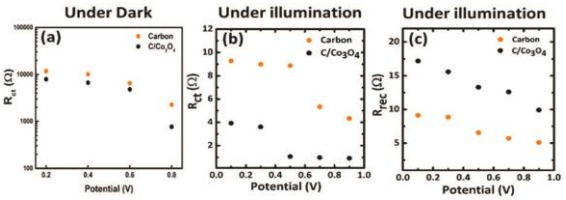

Fig. 5 (a) Charge transfer resistance (R_{ct}) vs. potential measurement of the carbon/perovskite solar cell with (Co_3O_4/C) and without Co_3O_4 (carbon) with an active area of 0.8 cm^2 in the dark, (b) charge transfer resistance (R_{ct}) vs. potential measurement of the carbon/perovskite solar cell with (Co_3O_4/C) and without Co_3O_4 (carbon) with an active area of 0.8 cm^2 under 1 sun illumination, (c) charge transfer resistance (R_{rec}) vs. potential measurement of the carbon/perovskite solar cell with (Co_3O_4/ C) and without Co_3O_4 (carbon) with an active area of 0.8 cm^2 under1 sun illumination.

Stability of the devices

Carbon has proven to be a good encapsulation for perovskite solar cells which reduces the degradation caused by a humid environment and improves the stability. We have analysed the performance and stability of carbon PSCs after the inclusion of the Co_3O_4 layer to enhance the hole extraction. Solar cells were exposed to an open environment (humidity levels of ~70% RH and room temperature 25 °C) for several weeks without any encapsulation and subsequently their performance was measured every week. Fig. 6a shows the normalized PCE of perovskite solar cells with and without Co_3O_4 (with an active area of 32 cm^2) measured under standard AM 1.5 illumination. From Fig. 6a, the device efficiency for perovskite cells with the Co_3O_4 layer remained unchanged remarkably for more than 100 days and the

devices showed no sign of degradation. The device efficiency for perovskite solar cells with carbon alone suffered a decrement of about 9% compared to Co_3O_4-based perovskite solar cells. The Co_3O_4 layer resists the moisture and provides an extra stability layer against the moisture along with the carbon.

To further confirm the reliability of PSCs, we measured the output current density of continuously illuminated Co_3O_4based perovskite solar cells (with an active area of 0.8 cm^2) by maximum power point tracking (MPPT) at a constant applied bias of 0.63 V (close to the maximum power point of the device). The J–V curve of the perovskite solar cell was measured under 1 sun before doing MPPT, which is plotted in Fig. S9.† This measurement was done by holding the solar cell at V_{mp} and monitoring the photocurrent until it stabilizes.[57] P_{mppt} of the perovskite solar cell is obtained using the following formula and plotted in Fig. 6b:

$$P_{mppt} = J_{mppt} \times V_{mp}/P_{in}$$

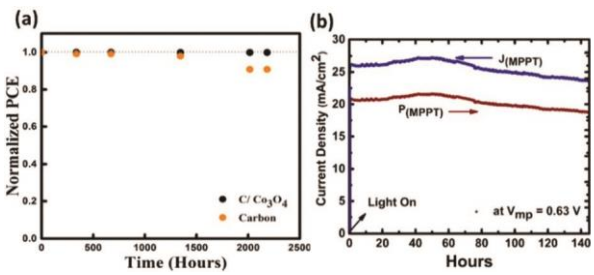

Fig. 6 (a) Normalized PCE for the standard perovskite solar cell containing carbon and a Co^1O_4 HTL measured under ambient environment conditions, and under standard AM 1 sun illumination. (b) Current density during the MPPT measurement of the Co_3O_4/carbon solar cell at V = 0.63 V measured under standard AM 1 sun illumination.

As shown in Fig. 6b the photocurrent density and the corresponding PCE rises quickly to a maximum value, and then stabilized within a few minutes. A slight increase in the current density was observed during the MPPT measurement. This is commonly attributed to the interaction of the perovskite layer with ambient humidity.[58] From the steady state photocurrent density (20.7 mA cm^{-2}), the stabilized PCE at 0.63 V is estimated to be 11.32%, which correlates well with the small hysteresis and matches the PCE value from the J–V curve. Perovskite modules show a degradation of less than 10% for continuous light soaking for 140 h. Thus, the carbon based perovskite solar cell with the Co_3O_4 interlayer shows high performance steadiness under ambient and light soaking conditions as well.

Conclusion

A chemical precipitation method without any surfactant was used to prepare spinel cobaltite oxide nanomaterials. The XRD and XAS observations demonstrate the presence of Co2+ and Co3+ states in the Co3O4 nanoparticles. The devices realized with the screen printed Co3O4 interlayer exhibited 18% more power conversion efficiency (PCE) of 13.27% as compared to standard carbon devices. The improvement in the overall

performance is attributed to the lower hole charge transfer resistance and reduced recombination at the interface, as proven by steady state and transient photoluminescence spectroscopy, and impedance measurements. We have scaled up the size of the PSCs from 0.09 cm2 to 70 cm2 with Co_3O_4 with a PCE of >11%. Hysteresis in the current–voltage characteristics was negligible; the PSCs remain stable after 2500 hours under ambient conditions. The enhanced device photovoltaic performance and stability are thoroughly discussed in this paper to show that cubic spinel Co_3O_4 is a very promising interlayer for fabricating efficient and stable carbon-based perovskite solar cells.

Experimental section

Materials

All chemicals were used as received without any purification.

Formation of Co_3O_4 paste

The paste for screen printing was formed by mixing 1 g of Co_3O_4 nanoparticles in a 100 mL mortar pot with 26 g ZrO_2 beads (0.3 mm diameter), 0.33 mL ethanol, 0.16 mL acetic acid and 0.16 mL deionized water. The resulting slush was subjected to ball milling at 450 rpm for 6 h. After grinding, the resulting slush was poured into 66.6 mL ethanol and stirred for 20 min. Then, the stirring was stopped and the suspension began to separate. After 10 min, the supernatant colloidal solution was separated and mixed with 10 g ethyl cellulose and 8 g terpineol. Finally, the whole colloidal solution was concentrated by rotary evaporation to obtain a Co_3O_4 paste for screen printing, containing 10% nanoparticles, 10% ethyl cellulose and 80% terpineol. The thickness of the original paste was 530 nm, which was further diluted with terpineol in different ratios (1 : 7, 1 : 5, 1 : 3) to obtain different thicknesses.

Solar cell device fabrication

Fluorine doped tin oxide (FTO, ~14 ohm per square, 2.2 mm thick) substrates were first etched with a CO_2 laser to form the desired pattern. Prior to deposition, the substrates were cleaned by ultrasonication in decon soap solution, followed by deionized water (DI water) and finally ethanol. The step was repeated twice. Each sonication process is held at 40 °C for 30 min. These substrates were then immersed in 50 mM of $TiCl_4$ solution (Wako Pure Chemical Industries, Ltd) for 30 min at 70 °C, followed by rinsing with DI water. The substrates were held at 500 °C for 30 min to allow the formation of TiO_2 crystals to serve as the seed layer. Using a screenprinter (MicroTec MT320TV), a layer of compact TiO_2 paste (Dyesol BL-1) was printed onto the substrate using a screen mask. The printed film was allowed to relax for 20 min before being calcined at 500 °C for 30 min. These substrates were finally immersed in 100 mM of $TiCl_4$ solution (Wako Pure Chemical Industries, Ltd) for 30 min at 70 °C to fill up the defective “pin-holes”, followed by rinsing with DI water. A final heat treatment of 500 °C completes the formation of the blocking layer. A 500 nm thick layer of a mesoporous TiO_2 film was printed onto the

substrate with a TiO_2 paste (Dyesol NRD-30, diluted with terpineol (Sigma, FG) in a weight ratio 1 : 1.4). Subsequently, the substrates were sintered for 30 min at 500 °C to improve the crystallinity. Then, a ZrO_2 (Solaronix, Zr-Nanoxide ZT/SP) spacer layer was printed on top of the meso-TiO_2 layer and heated to 500° C for 30 min to remove the binders (ethyl cellulose). On top of ZrO_2, a very thin layer (70 nm) of Co_3O_4 was applied as an HTL, and the film was sintered at 500 °C for 30 min. Finally, carbon paste (Dyesol) was printed on top of ZrO_2 to complete the triple layer device stack. The substrates were heated at 400 °C for 30 min. A perovskite solution was obtained by mixing an equimolar ratio of PbI_2 and CH_3HN_3I (Tokyo Chemical Limited) in γ-butyrolactone (Sigma, ≥99%). 5 AVA-I prepared by reacting 5-aminovaleric acid (Sigma) with hydroiodic acid (Sigma) in an equimolar ratio, followed by filtering and purification. 5 AVA-I was added to the perovskite solutions in a molar ratio of 1 : 20 (AVA-I to MAI). The solutions are kept stirring overnight on a 50 °C hotplate for complete dissolution of the precursors. The perovskite solution was dropped on the carbon layer using a micropipette. For small devices with an active area of 0.8 cm^2, we used 4.0 μL of perovskite solution, while for modules we used approximately 21–24 μL per strip.

Characterization

Thin film X-ray diffraction data were collected by using a Bruker D8 Advance diffractometer using Cu Kα radiation. The thickness of the printed film is measured by using a surface profiler (NanoMap-500LS, AEP technology). X-ray absorption fine structure (XAFS) characterization at the Co K edge (7709 eV) was carried out at the XAFCA beamline of the Singapore Synchrotron Light Source (SSLS). The X-ray energy was calibrated at the inflection point of the absorption edge of cobalt foil. Data analysis was carried out with Athena and Artemis included in the Demeter package. The powder sample was prepared in a pellet using a pelletizer of diameter 12 mm and mounted on the sample holder for XAS measurement. Usually around 7 mg of sample was mixed with 50 mg of BN to make the pellet. The XANES analysis shows the oxidation state and the white line intensity difference between the sample and the reference compound used to analyze the sample. In this case, $CoSO_4$ was used as the reference standard for the Co_3O_4 sample. The FE-SEM images were acquired using a Jeol JSM-7600F field emission scanning electron microscope. HRTEM analysis was performed using JEOL TEM 2010 and 2100F. To study the TRPL decay, the micro-PL setup used a fiber coupled microscope system, with a VIS-NIR microscope objective (10×, NA = 0.65). The samples were excited by a picosecond-pulse light emitting diode at 405 nm (Picoquant P-C-405B) with a 5 MHz repetition rate. The beam spot size was ~10 mm. The TRPL decays were collected with an Acton mono-chromator (SpectraPro 2300), fiber coupled to the microscope, and detected by using a Micro Photon Devices single photon avalanche photodiode. The signal was then received by a time-correlated single

photon counting card. The temporal resolution is ~5 picoseconds. To measure MPPT, an Autolab machine (PGSTAT302N, Software version-NOVA 1.11) was used to apply the voltage and measure the current, while the samples were illuminated with a white LED light source. I–V characteristics of the devices were determined using the solar simulator (San-EI Electric, XEC-301S) quipped with a 450 W xenon lamp connected to a Keithley 2612A source meter. The power of the simulated light was calibrated using a Si reference cell (Fraunhofer) and monitored using a power meter throughout the testing. Impedance spectroscopy was performed using an Autolab potentiostat (PGSTAT 302). A voltage perturbation of 20 mV was applied from 400 kHz to 1 Hz at different bias voltages.

Conflicts of interest

There are no conflicts to declare.

Acknowledgements

The authors would like to express their appreciation to Prof. Cesare Soci for access to the TRPL equipment in his laboratory. This research was supported by the National Research Foundation, Prime Minister's Office, Singapore under its Competitive Research Programme (CRP Award no. NRF-CRP142014-03) and through the Singapore – Berkeley Research Initiative for Sustainable Energy (SinBeRISE) CREATE Program".

References

1 M. A. Green, A. Ho-Baillie and H. J. Snaith, The emergence of perovskite solar cells, Nat. Photonics, 2014, 8, 506–514.

2 S. A. Veldhuis, P. P. Boix, N. Yantara, M. Li, T. C. Sum, N. Mathews and S. G. Mhaisalkar, Perovskite materials for light-emitting diodes and lasers, Adv. Mater., 2016, 28, 6804–6834.

3 S. D. Stranks and H. J. Snaith, Metal-halide perovskites for photovoltaic and light-emitting devices, Nat. Nanotechnol., 2015, 10, 391–402.

4 G. Xing, N. Mathews, S. Sun, S. S. Lim, Y. M. Lam, M. Grätzel, S. Mhaisalkar and T. C. Sum, Long-range balanced electron-and hole-transport lengths in organic-inorganic CH3NH3PbI3, Science, 2013, 342, 344–347.

5 T. M. Brenner, D. A. Egger, L. Kronik, G. Hodes and D. Cahen, Hybrid organic—inorganic perovskites: low-cost semiconductors with intriguing charge-transport properties, Nat. Rev. Mater., 2016, 1, 15007.

6 D. Shi, V. Adinolfi, R. Comin, M. Yuan, E. Alarousu,A. Buin, Y. Chen, S. Hoogland, A. Rothenberger, K. Katsiev, Y. Losovyj, X. Zhang, P. A. Dowben, O. F. Mohammed, E. H. Sargent and O. M. Bakr, Low trap-state density and long carrier diffusion in organic lead trihalide perovskite single crystals, Science, 2015, 347, 519.

7 Q. Dong, Y. Fang, Y. Shao, P. Mulligan, J. Qiu, L. Cao and J. Huang, Electron-hole diffusion lengths >175 μm in solution-grown $CH_3NH_3PbI_3$ single crystals, Science, 2015, 347, 967–970.

8 J. S. Manser, J. A. Christians and P. V. Kamat, Intriguing Optoelectronic Properties of Metal Halide Perovskites, Chem. Rev., 2016, 116, 12956–13008.

9 S. Shukla, S. Shukla, L. J. Haur, S. S. Dintakurti, G. Han, A. Priyadarshi, T. Baikie, S. G. Mhaisalkar and N. Mathews, Effect of Formamidinium/Cesium Substitution and PbI2 on the Long-Term Stability of Triple-Cation Perovskites, ChemSusChem, 2017, 10, 3804–3809.

10 (a) M. A. Green, Corrigendum to 'Solar cell efficiency tables (version 49)', Prog. Photovolt: Res. Appl., 2017, 25, 3–13; (b) M. A. Green, Corrigendum to 'Solar cell efficiency tables (version 49)', Prog. Photovolt: Res. Appl., 2017, 4, 333–334.

11 P. P. Boix, K. Nonomura, N. Mathews and S. G. Mhaisalkar, Current progress and future perspectives for organic/inorganic perovskite solar cells, Mater. Today, 2014, 17, 16–23.

12 N. J. Jeon, J. H. Noh, Y. C. Kim, W. S. Yang, S. Ryu and S. I. Seok, Solvent engineering for high-performance inorganic–organic hybrid perovskite solar cells, Nat. Mater., 2014, 13, 897–903.

13 J. Shi, X. Xu, D. Li and Q. Meng, Interfaces in Perovskite Solar Cells, Small, 2015, 11, 2472–2486.

14 W. Nie, H. Tsai, R. Asadpour, J.-C. Blancon, A. J. Neukirch,
G. Gupta, J. J. Crochet, M. Chhowalla, S. Tretiak, M. A. Alam, H.-L. Wang and A. D. Mohite, High-efficiency solution-processed perovskite solar cells with millimeterscale grains, Science, 2015, 347, 522.

15 M. Yang, T. Zhang, P. Schulz, Z. Li, G. Li, D. H. Kim, N. Guo, J. J. Berry, K. Zhu and Y. Zhao, Facile fabrication of large-grain CH3NH3PbI3−xBrx films for high-efficiency solar cells via CH3NH3Br-selective Ostwald ripening, Nat. Commun., 2016, 7, 12305.

16 M. Saliba, T. Matsui, J.-Y. Seo, K. Domanski, J.-P. CorreaBaena, M. K. Nazeeruddin, S. M. Zakeeruddin, W. Tress, A. Abate, A. Hagfeldt and M. Gratzel, Cesium-containing triple cation perovskite solar cells: improved stability, reproducibility and high efficiency, Energy Environ. Sci., 2016, 9, 1989–1997.

17 H. Tan, A. Jain, O. Voznyy, X. Lan, F. P. G. de Arquer,
J. Z. Fan, R. Quintero-Bermudez, M. Yuan, B. Zhang and Y. Zhao, Efficient and stable solution-processed planar perovskite solar cells via contact passivation, Science, 2017, 355, 722–726.

18 Y. H. Lee, J. Luo, M.-K. Son, P. Gao, K. T. Cho, J. Seo, S. M. Zakeeruddin, M. Grätzel and M. K. Nazeeruddin, Enhanced Charge Collection with Passivation Layers in Perovskite Solar Cells, Adv. Mater., 2016, 28, 3966– 3972.

19 X. Li, M. Ibrahim Dar, C. Yi, J. Luo, M. Tschumi,

S. M. Zakeeruddin, M. K. Nazeeruddin, H. Han and
M. Grätzel, Improved performance and stability of perovskite solar cells by crystal crosslinking with alkylphosphonic acid ω-ammonium chlorides, Nat. Chem., 2015, 7, 703–711.

20 A. Mei, X. Li, L. Liu, Z. Ku, T. Liu, Y. Rong, M. Xu, M. Hu, J. Chen and Y. Yang, A hole-conductor–free, fully printable mesoscopic perovskite solar cell with high stability, Science, 2014, 345, 295–298.

21 A. Priyadarshi, L. J. Haur, P. Murray, D. Fu, S. Kulkarni, G. Xing, T. C. Sum, N. Mathews and S. G. Mhaisalkar, A large area (70 cm2) monolithic perovskite solar module with a high efficiency and stability, Energy Environ. Sci., 2016, 9, 3687–3692.

22 X. Li, M. Tschumi, H. Han, S. S. Babkair, R. A. Alzubaydi,

A. A. Ansari, S. S. Habib, M. K. Nazeeruddin,

S. M. Zakeeruddin and M. Grätzel, Outdoor Performanceand Stability under Elevated Temperatures and Long-Term Light Soaking of Triple-Layer Mesoporous Perovskite Photovoltaics, Energy Technol., 2015, 3, 551–555.

23 Y. Rong, X. Hou, Y. Hu, A. Mei, L. Liu, P. Wang and H. Han, Synergy of ammonium chloride and moisture on perovskite crystallization for efficient printable mesoscopic solar cells, Nat. Commun., 2017, 8, 14555.

24 A. Priyadarshi, A. Bashir, J. T. Gunawan, L. J. Haur, A. Bruno, Z. Akhter, N. Mathews and S. G. Mhaisalkar, Simplified Architecture of a Fully Printable Perovskite Solar Cell Using a Thick Zirconia Layer, Energy Technol., 2017, 5, 1866–1872.

25 V. Kapoor, A. Bashir, L. J. Haur, A. Bruno, S. Shukla, A. Priyadarshi, N. Mathews and S. Mhaisalkar, Effect of Excess PbI2 in Fully Printable Carbon-based Perovskite Solar Cells, Energy Technol., 2017, 5, 1880–1886.

26 J. Li, G. Niu, W. Li, K. Cao, M. Wang and L. Wang, Insight into the CH3NH3PbI3/C interface in hole-conductor-free mesoscopic perovskite solar cells, Nanoscale, 2016, 8, 14163–14170.

27 Z. Liu, M. Zhang, X. Xu, L. Bu, W. Zhang, W. Li, Z. Zhao, M. Wang, Y.-B. Cheng and H. He, p-Type mesoscopic NiO as an active interfacial layer for carbon counter electrode based perovskite solar cells, Dalton Trans., 2015, 44, 3967– 3973.

28 Z. Liu, M. Zhang, X. Xu, F. Cai, H. Yuan, L. Bu, W. Li, A. Zhu, Z. Zhao and M. Wang, NiO nanosheets as efficient top hole transporters for carbon counter electrode based perovskite solar cells, J. Mater. Chem. A, 2015, 3, 24121– 24127.

29 X. Xu, Z. Liu, Z. Zuo, M. Zhang, Z. Zhao, Y. Shen, H. Zhou, Q. Chen, Y. Yang and M. Wang, Hole selective NiO contact for efficient perovskite solar cells with carbon electrode, Nano Lett., 2015, 15, 2402–2408.

30 S. A. Makhlouf, Z. H. Bakr, K. I. Aly and M. Moustafa, Structural, electrical and optical properties of Co 3 O 4 nanoparticles, Superlattices Microstruct., 2013, 64, 107–117.

31 X. Shi, S. L. Bernasek and A. Selloni, Oxygen Deficiency and Reactivity of Spinel NiCo2O4 (001) Surfaces, J. Phys. Chem. C, 2017, 121, 3929–3937.

32 K. P. Reddy, R. Jain, M. K. Ghosalya and C. S. Gopinath, Metallic Cobalt to Spinel Co3O4 Electronic Structure Evolution by Near-Ambient Pressure Photoelectron

Spectroscopy, J. Phys. Chem. C, 2017, 121, 21472–21481.

33 P. F. Ndione, A. Garcia, N. E. Widjonarko, A. K. Sigdel, K. X. Steirer, D. C. Olson, P. A. Parilla, D. S. Ginley, N. R. Armstong and R. E. Richards, Highly-Tunable Nickel Cobalt Oxide as a Low-Temperature P-Type Contact in Organic Photovoltaic Devices, Adv. Energy Mater., 2013, 3, 524–531.

34 M. Langell, M. Anderson, G. Carson, L. Peng and S. Smith, Valence-band electronic structure of Co 3 O 4 epitaxy on CoO (100), Phys. Rev. B: Condens. Matter Mater. Phys., 1999, 59, 4791.

35 F. Zhang, C. Yuan, X. Lu, L. Zhang, Q. Che and X. Zhang, Facile growth of mesoporous Co 3 O 4 nanowire arrays on Ni foam for high performance electrochemical capacitors, J. Power Sources, 2012, 203, 250–256.

36 A. Xiao, S. Zhou, C. Zuo, Y. Zhuan and X. Ding, Controllable synthesis of mesoporous Co 3 O 4 nanoflake array and its application for supercapacitor, Mater. Res. Bull., 2014, 60, 674–678.

37 J. Xu, L. Gao, J. Cao, W. Wang and Z. Chen, Preparation and electrochemical capacitance of cobalt oxide (Co 3 O 4) nanotubes as supercapacitor material, Electrochim. Acta, 2010, 56, 732–736.

38 D. Zhang and W. Zou, Decorating reduced graphene oxide with Co 3 O 4 hollow spheres and their application in supercapacitor materials, Curr. Appl. Phys., 2013, 13, 1796– 1800.

39 X. Liu, G. Qiu and X. Li, Shape-controlled synthesis and properties of uniform spinel cobalt oxide nanocubes, Nanotechnology, 2005, 16, 3035.

40 T. He, D. Chen, X. Jiao, Y. Wang and Y. Duan, Solubilitycontrolled synthesis of high-quality Co3O4 nanocrystals, Chem. Mater., 2005, 17, 4023–4030.

41 O. Galović, M. Samardžić, S. Petrušić and M. Sak-Bosnar, Application of a new potentiometric sensor for determination of anionic surfactants in wastewater, Chem. Biochem. Eng. Q., 2015, 29, 307–313.

42 S. Deng, X. Xiao, G. Chen, L. Wang and Y. Wang, Cd doped porous Co 3 O 4 nanosheets as electrode material for high performance supercapacitor application, Electrochim. Acta, 2016, 196, 316–327.

43 Y. Du, Y. Zhu, S. Xi, P. Yang, H. O. Moser, M. B. Breese and A. Borgna, XAFCA: a new XAFS beamline for catalysis research, J. Synchrotron Radiat., 2015, 22, 839–843.

44 I. S. Kotousova and S. M. Polyakov, Electron-diffraction study of Co_3O_4, Kristallografiya, 1972, 17, 661–663.

45 M. Lelis, A. Porto, C. Goncalves and J. Fabris, Cation occupancy sites in synthetic Co-doped magnetites as determined with X-ray absorption (XAS) and Mössbauer spectroscopies, J. Magn. Magn. Mater., 2004, 278, 263–269.

46 T. Jiang and D. Ellis, X-ray absorption near edge structures in cobalt oxides, J. Mater. Res., 1996, 11, 2242–2256.

47 C.-S. Cheng, M. Serizawa, H. Sakata and T. Hirayama, Electrical conductivity of Co 3 O 4 films prepared by chemical vapour deposition, Mater. Chem. Phys., 1998, 53,

225–230. 48 S. van Reenen, M. Kemerink and H. J. Snaith, Modeling Anomalous Hysteresis in Perovskite Solar Cells, J. Phys. Chem. Lett., 2015, 6, 3808–3814.

49 D. W. Miller, G. E. Eperon, E. T. Roe, C. W. Warren, H. J. Snaith and M. C. Lonergan, Defect states in perovskite solar cells associated with hysteresis and performance, Appl. Phys. Lett., 2016, 109, 153902.

50 P. Calado, A. M. Telford, D. Bryant, X. Li, J. Nelson, B. C. O'Regan and P. R. F. Barnes, Evidence for ion migration in hybrid perovskite solar cells with minimal hysteresis, Nat. Commun., 2016, 7, 13831.

51 Y. Yang, J. Xiao, H. Wei, L. Zhu, D. Li, Y. Luo, H. Wu and Q. Meng, An all-carbon counter electrode for highly efficient hole-conductor-free organo-metal perovskite solar cells, RSC Adv., 2014, 4, 52825–52830.

J. B. J. Kim, D. H. Kim, Y.-Y. Lee, H.-W. Shin, G. S. Han, S. Hong, K. Mahmood, T. K. Ahn, Y.-C. Joo and S. Hong, Highly efficient and bending durable perovskite solar cells: toward a wearable power source, Energy Environ. Sci., 2015, 8, 916–921.

52 Q. Wang, J.-E. Moser and M. Grätzel, Electrochemical impedance spectroscopic analysis of dye-sensitized solar cells, J. Phys. Chem. B, 2005, 109, 14945–14953.

53 H. Chen, Z. Wei, H. He, X. Zheng, K. S. Wong and S. Yang, Solvent Engineering Boosts the Efficiency of Paintable Carbon-Based Perovskite Solar Cells to Beyond 14%, Adv. Energy Mater., 2016, 6, 1502087.

54 S. N. Habisreutinger, T. Leijtens, G. E. Eperon, S. D. Stranks, R. J. Nicholas and H. J. Snaith, Enhanced hole extraction in perovskite solar cells through carbon nanotubes, J. Phys. Chem. Lett., 2014, 5, 4207–4212.

55 J. Ryu, K. Lee, J. Yun, H. Yu, J. Lee and J. Jang, Paintable Carbon-Based Perovskite Solar Cells with Engineered Perovskite/Carbon Interface Using Carbon Nanotubes Dripping Method, Small, 2017, 13, 170225.

56 J. A. Christians, J. S. Manser and P. V. Kamat, Best practices in perovskite solar cell efficiency measurements. Avoiding the error of making bad cells look good, ACS Publications, 2015.

57 S. G. Hashmi, D. Martineau, M. I. Dar, T. T. T. Myllymäki, T. Sarikka, V. Ulla, S. M. Zakeeruddin and M. Grätzel, High performance carbon-based printed-perovskite solar cells with humidity assisted thermal treatment, J. Mater. Chem. A, 2017, 5, 12060–12067.